Journal of Applied Mechanics and Technical Physics, Vol. 47, No. 1, pp. 127–133, 2006

MOMENT OF RESISTANCE OF A DISK ROTATING IN A CLOSED AXISYMMETRIC CAVITY

K. N. Volkov

UDC 532.529:536.24

A turbulent flow in a closed axisymmetric cavity with a rotating disk is considered. The moment of resistance to disk rotation is calculated as a function of the dimensionless gap between the motionless casing and rotating disk and of the Reynolds number. Results calculated on the basis of different turbulence models are compared with data of a physical experiment and with available correlations.

Key words: *turbulence, rotation, moment, internal flows.*

Introduction. Design of advanced gas-turbine engines is almost impossible without using numerical methods for calculating internal turbulent flows and heat transfer of a viscous compressible gas in complicated geometric configurations. The validity of using particular turbulence models and numerical methods is normally tested on simpler problems, which have simpler geometry but retain the key aspects of the initial formulation, e.g., flow swirl or rotation of one or several boundary surfaces.

One of such problems is the flow in a closed axisymmetric cavity with a rotating disk. This problem has been intensely addressed in the literature [1–10] because of the simple geometry and still rather complicated flow caused, in particular, by formation of the Ekman layers on the rotating disk and by heat transfer.

Four flow regimes are identified [1–3] depending on the dimensionless gap $G = s/b$ (Fig. 1) between the casing (stator) and disk (rotor) and on the Reynolds number $\mathrm{Re} = \omega b^2/\nu$ based on the angular velocity ω and disk radius b (Fig. 2).

Regime I corresponds to rather small gaps; the thickness of the laminar boundary layers on the stator and rotor approximately equals the half-width of the cavity (the boundary layers on the stator and rotor merge), and the action of viscous forces extends to the entire computational domain. In regime II, the laminar boundary layers on the stator and rotor are separated by a liquid layer in which the effect of viscosity is rather low. In contrast to regime I, the tangential component of velocity in the core flow is independent of the axial coordinate, and the radial component of velocity is almost zero.

Regimes III and IV are equivalent to regimes I and II, except for the fact that the boundary layers on the stator and rotor are turbulent.

The main contribution to changes in velocity of the liquid in regimes II and IV is made by the Ekman layers formed on the walls orthogonal to the axis of rotation [4].

In some cases, the use of the approximation of a freely rotating disk is sufficient to find the integral characteristics of the flow. For turbomachinery wheels rotating in narrow shrouds whose width is small as compared to the disk radius, however, the free-disk approximation is inapplicable and yields large errors [4].

In regime I (with $\mathrm{Re} < 10^4$), the moment coefficient is evaluated theoretically; approximate estimates are obtained in regimes II (with $\mathrm{Re} < 10^5$) and III [4]. The estimates for regimes II and III are independent of the shroud width and yield moment coefficients that are 16% lower than the measured values.

The following correlations (for two sides of the disk) are available for estimating the moment coefficient for $\mathrm{Re} < 10^7$ [1, 5]:

University of Surrey, Guildford, UK; dsci@mail.ru. Translated from Prikladnaya Mekhanika i Tekhnicheskaya Fizika, Vol. 47, No. 1, pp. 153–160, January–February, 2006. Original article submitted January 18, 2005.

0021-8944/06/4701-0127

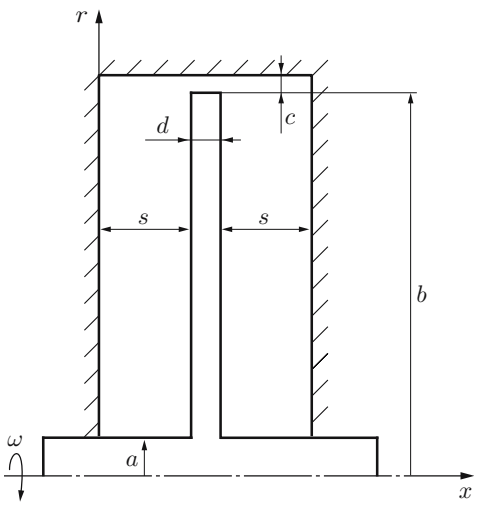

Fig. 1

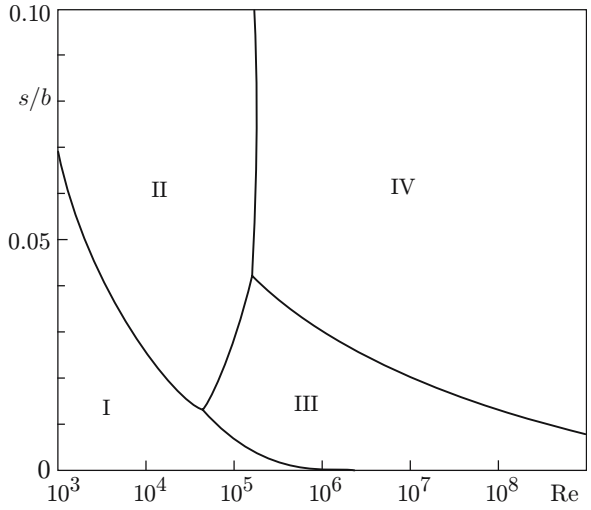

Fig. 2

Fig. 1. Geometry of the computational domain.

Fig. 2. Flow regimes in a cavity with a rotating disk.

$$C_M = \begin{cases} 1.850\, G^{1/10}\, \mathrm{Re}^{-1/2} & \text{in regime II,} \\ 0.040\, G^{-1/6}\, \mathrm{Re}^{-1/4} & \text{in regime III,} \\ 0.051\, G^{1/10}\, \mathrm{Re}^{-1/5} & \text{in regime IV.} \end{cases}$$

The corrected dependences [2] differ from those given above only by the constants (0.036 in regime III and 0.0545 in regime IV).

In regime III, the moment coefficient depends to a significant extent on the distance between the stator and rotor. In regime IV with large values of G, the moment coefficient tends to the limiting value for the free disk [3]. The minimum value of the moment corresponds to the point of transition from regime III to regime IV (at $G_* = 0.211\,\mathrm{Re}^{-3/16}$). The critical value of the gap is temperature-dependent [6].

One problem that arises in numerical simulations of turbulent flows at high Reynolds numbers is the choice of an appropriate turbulence model. Examples of using some turbulence models can be found in [7–10].

The use of the standard k–ε model and k–ω model yields rather large errors in velocity distributions in the central part of the cavity and overestimated thickness of the boundary layers on the stator and rotor [7]. The low-Reynolds-number version of the k–ε model reveals unrealistic trends to flow laminarization in the cavity [8]. The Launder–Sharma modification of the k–ε model does not always produce acceptable results either [9]. The accuracy of calculations is normally improved by using empirical corrections to the equation for the dissipation rate of the turbulent kinetic energy [9], a two-layer turbulence model [7], and a model of the Reynolds stress transport [10].

The challenge of the present activity is to numerically simulate the flow in a closed axisymmetric cavity with a rotating disk with the use of different turbulence models and to compare the moment coefficients calculated within different models with the data of a physical experiment and available correlations.

Governing Equations. In a cylindrical coordinate system (x, r, θ), the unsteady motion of a viscous compressible gas, which is induced by rotation of a disk of radius b with a constant angular velocity ω around the axis perpendicular to the disk plane (Fig. 1), is described by the equation

$$\frac{\partial \boldsymbol{Q}}{\partial t} + \frac{\partial\,(\boldsymbol{F}_x + \boldsymbol{G}_x)}{\partial x} + \frac{1}{r}\,\frac{\partial r\,(\boldsymbol{F}_r + \boldsymbol{G}_r)}{\partial r} = \boldsymbol{H}$$

supplemented by the equation of state of a perfect gas

$$p = (\gamma - 1)\rho[E - (v_x^2 + v_r^2 + v_\theta^2 - \omega^2 r^2)/2].$$

The vector of conservative variables $\boldsymbol{Q}$, the vector of inviscid fluxes $\boldsymbol{F}$, the vector of viscous fluxes $\boldsymbol{G}$, and the source term $\boldsymbol{H}$ have the following form:

$$\boldsymbol{Q} = \begin{pmatrix} \rho \\ \rho v_x \\ \rho v_r \\ \rho v_\theta \\ \rho E \end{pmatrix}, \qquad \boldsymbol{F}_x = \begin{pmatrix} \rho v_x \\ \rho v_x v_x + p \\ \rho v_x v_r \\ \rho v_x v_\theta \\ (\rho E + p) v_x \end{pmatrix}, \qquad \boldsymbol{F}_r = \begin{pmatrix} \rho v_r \\ \rho v_r v_x \\ \rho v_r v_r + p \\ \rho v_r v_\theta \\ (\rho E + p) v_r \end{pmatrix},$$

$$\boldsymbol{G}_x = -\begin{pmatrix} 0 \\ \tau_{xx} \\ \tau_{xr} \\ \tau_{x\theta} \\ v_x\tau_{xx} + v_\theta\tau_{x\theta} + v_r\tau_{xr} - q_x \end{pmatrix}, \quad \boldsymbol{G}_r = -\begin{pmatrix} 0 \\ \tau_{rx} \\ \tau_{rr} \\ \tau_{r\theta} \\ v_x\tau_{rx} + v_\theta\tau_{r\theta} + v_r\tau_{rr} - q_r \end{pmatrix},$$

$$\boldsymbol{H} = \frac{1}{r}\begin{pmatrix} 0 \\ 0 \\ p - \tau_{\theta\theta} + \rho(v_\theta - r\,\omega)^2 \\ \tau_{r\theta} - \rho v_r(v_\theta - 2r\,\omega) \\ 0 \end{pmatrix}.$$

In addition to terms related to the axisymmetric formulation of the problem, the source term $\boldsymbol{H}$ takes into account the action of inertia forces (Coriolis force and centrifugal force). The components of the viscous stress tensor are found from the relations

$$\tau_{xx} = 2\mu_e \frac{\partial v_x}{\partial x} - \frac{2}{3}\mu_e\Big(\frac{\partial v_x}{\partial x} + \frac{1}{r}\frac{\partial r v_r}{\partial r}\Big), \qquad \tau_{x\theta} = \tau_{\theta x} = \mu_e \frac{\partial v_\theta}{\partial x},$$

$$\tau_{rr} = 2\mu_e \frac{\partial v_r}{\partial r} - \frac{2}{3}\mu_e\Big(\frac{\partial v_x}{\partial x} + \frac{1}{r}\frac{\partial r v_r}{\partial r}\Big), \qquad \tau_{xr} = \tau_{rx} = \mu_e\Big(\frac{\partial v_r}{\partial x} + \frac{\partial v_x}{\partial r}\Big),$$

$$\tau_{\theta\theta} = 2\mu_e \frac{v_r}{r} - \frac{2}{3}\mu_e\Big(\frac{\partial v_x}{\partial x} + \frac{1}{r}\frac{\partial r v_r}{\partial r}\Big), \qquad \tau_{r\theta} = \tau_{\theta r} = \mu_e\Big(\frac{\partial v_\theta}{\partial r} - \frac{v_\theta}{r}\Big).$$

The components of the heat-flux vector are

$$q_x = -\lambda_e \frac{\partial T}{\partial x}, \qquad q_r = -\frac{\lambda_e}{r}\frac{\partial r T}{\partial r}.$$

In the above-given equations, t is the time, ρ is the gas density, v_x, v_r, and v_θ are the velocity components in the coordinate directions x, r, and θ, respectively, p is the pressure, E is the total energy per unit mass, T is the temperature, and γ is the ratio of specific heats.

The effective viscosity and thermal conductivity are the sum of molecular and turbulent transport coefficients

$$\mu_e = \mu + \mu_{\rm t}, \qquad \lambda_e = c_p(\mu/{\rm Pr} + \mu_{\rm t}/{\rm Pr}_{\rm t}),$$

where c_p is the thermal conductivity at constant pressure. The turbulent Prandtl number is assigned a constant value (${\rm Pr}_{\rm t} = 0.9$ for air).

Molecular viscosity and temperature are related by Sutherland's law

$$\frac{\mu}{\mu_*} = \Big(\frac{T}{T_*}\Big)^{3/2}\frac{T_* + S_0}{T + S_0},$$

where $\mu_* = 1.68 \cdot 10^{-5}$ kg/(m $\cdot$ sec); $T_* = 273$ K and $S_0 = 110.5$ K for air. Molecular thermal conductivity is related to the Prandtl number (${\rm Pr} = 0.72$ for air).

Turbulence Models. The following turbulence models are used to calculate turbulent viscosity (or quantities related to it).

1. The standard k–ε turbulence model in the Launder–Spalding formulation [11] with the Kato–Launder correction for the term related to turbulence generation [12]. To take into account the curvature of streamlines and rotation, the formula for turbulent viscosity is supplemented by a damping function [13] depending on the turbulent Richardson number. The method of the near-wall functions [11] is used for the turbulent characteristics to impose the boundary conditions on the wall.

2. The two-layer k–ε/k–l turbulence model [14]. The near-wall domain is divided into two subdomains; the position of the interface between these subdomains depends on the local Reynolds number $\mathrm{Re}_y = \rho k^{1/2} y/\mu$. The standard k–ε model is used for $\mathrm{Re}_y > \mathrm{Re}_{y*}$, and the one-parameter k–l turbulence model is used for $\mathrm{Re}_y < \mathrm{Re}_{y*}$. It is assumed that $\mathrm{Re}_{y*} = 180$, and the boundary condition on the wall is $\partial k/\partial n = 0$.

3. The k–ω turbulence model [15]. Boundary conditions corresponding to the low-Reynolds-number formulation are set on the solid wall.

4. The Spalart–Allmaras model of turbulent viscosity (SA1) [16]. Vorticity is used to calculate the source term related to generation of turbulent viscosity. A modified form of the source term is also used (SA2) [17]. The method of the near-wall functions is used for the operating variable in formulating the boundary conditions on the wall [18].

5. The model of the Reynolds stress transport (RSM) [19], which takes into account the effect of streamline curvature and rotation without introduction of any additional empirical corrections.

Initial and Boundary Conditions. It is assumed that the gas is at rest at the initial time ($v_x = v_r = v_\theta = 0$, $p = 1.013 \cdot 10^5$ Pa, and $T = 288$ K). The stator and rotor surfaces are subject to the no-slip and no-penetration boundary conditions for the normal and tangential components of velocity, and the pressure is determined from the equation of momentum changes in the projection onto the normal to the wall. The stator and rotor are assumed to have a constant temperature.

Numerical Method. Discretization of the Navier–Stokes equations and equations of the turbulence model is performed by a finite-volume method on a nonuniform grid. The second-order Adams–Bashforth scheme is used for discretization of derivatives in time. The flux vector is split into the inviscid and viscid components. Discretization of convective fluxes is performed on the basis of the third-order MUSCL scheme (with a minmod flux limiter). The second-order centered finite-difference formulas are used for discretization of diffuse fluxes. Systems of difference equations are solved by a multigrid method based on the full approximation scheme (four grid levels and a V-cycle are used).

The computational grid contains 120 nodes in the axial direction and 2200 nodes in the radial direction (if the cavity width is changed, the number of nodes along the x and r coordinates is changed so that an acceptable ratio of the grid-cell sides is retained). The grid is refined both near the disk surface and near the casing surface. The nodes along the radial coordinate are distributed uniformly. There are about 10 computational cells in the region $y^+ < 15$. If the two-layer turbulence model is used, the grid is constructed so that $y^+ \sim 1$.

Computation Results. To compare the computed results with the data of a physical experiment [1], the flow parameters were assigned the following values: $G = 0.0637$, $b = 0.5$ m, $\omega = 257$ 1/sec, $T_1 = 300$ K, and $T_2 = 300$–450 K. The operating medium was air with $\rho_0 = 1.225$ kg/m^3 and $\mu_0 = 1.7894 \cdot 10^{-5}$ kg/(m $\cdot$ sec). Under these conditions,the Reynolds number is $\mathrm{Re} = 4.4 \cdot 10^6$. The subscripts 1 and 2 refer to the stator and rotor, respectively.

Figure 3 shows the radial and tangential components of velocity, which are obtained on the basis of different turbulence models and compared with the experimental data of [1] (points 1). The computed distributions are in fairly good agreement with the experimental data, except for the core flow where the radial velocity differs from zero in [1]. This effect contradicts the theory and is a consequence of measurement inaccuracy rather than a real physical phenomenon.

Rotation exerts a significant effect on turbulence characteristics. The data obtained on the basis of the k–ω model and two-layer k–ε/k–l turbulence model show that the distribution of the turbulent kinetic energy has two maximums near the stator and rotor surfaces (Fig. 4), which agrees with the data of [7]. The maximum of turbulent kinetic energy generation is located at a distance of $y^+ \sim 22$ from the surface in the stator boundary layer and at a distance of $y^+ \sim 6$ from the surface in the rotor boundary layer. Practically no turbulence generation occurs in the core flow in which there are no gradients of the mean flow velocity. The maximum value of the turbulent kinetic energy in the boundary layer on the rotor surface is approximately twice the corresponding value in the boundary layer on the stator surface.

The friction moment is found by integrating the shear stresses over the disk surface

$$M = -2\pi \int_a^b r^2 \tau_{x\theta}\, dr,$$

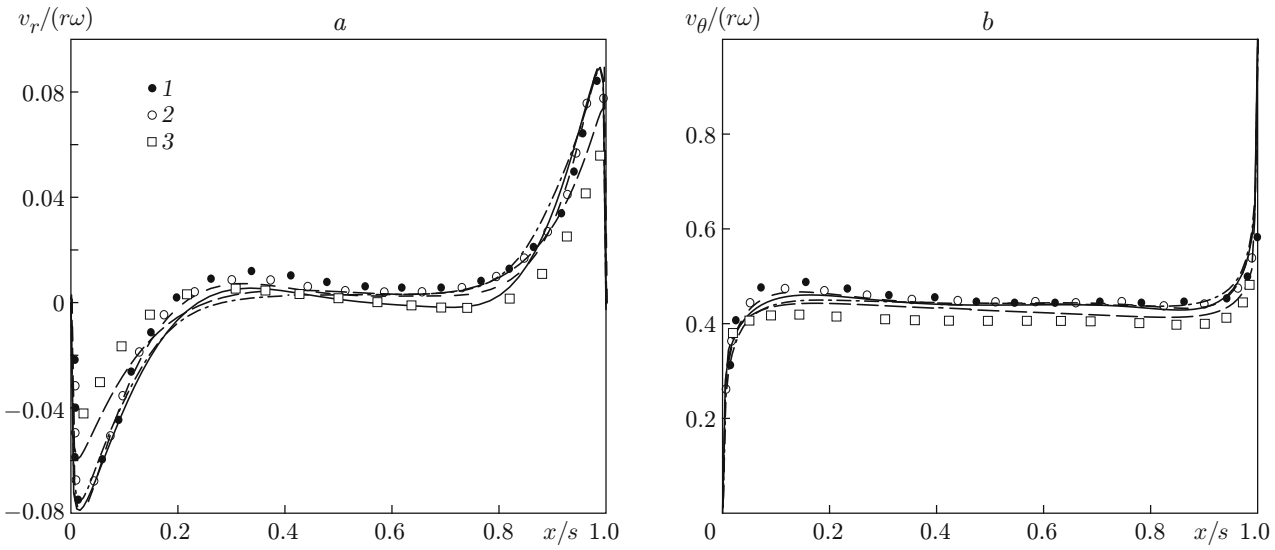

Fig. 3. Distributions of the radial (a) and tangential (b) components of velocity in the gap between the stator and rotor for $r/b = 0.765$: points 1 show the experimental data of [1]; other points and curves refer to computations by the k–ε model (solid curves), Spalart–Allmaras model (long-dashed curves), k–ω model (dash-and-dotted curves), Reynolds stress model (short-dashed curves), two-layer model (points 2), and modified Spalart–Allmaras model (points 3).

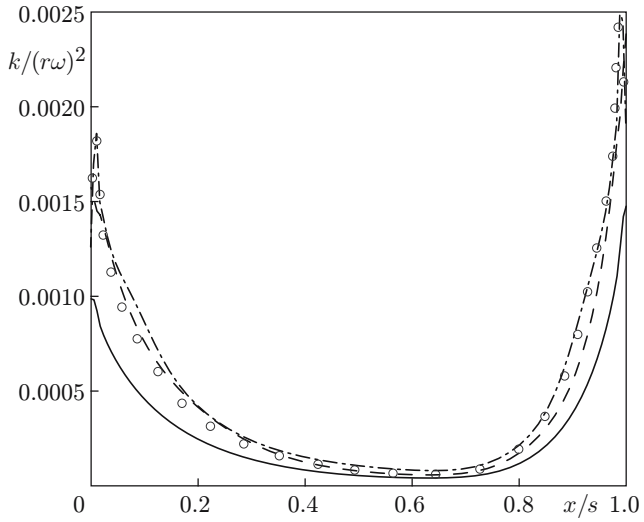

Fig. 4. Distributions of the turbulent kinetic energy in the gap between the stator and rotor for $r/b = 0.765$ (notation the same as in Fig. 3).

where $\tau_{x\theta}$ is the circumferential component of the shear friction on the wall. The resistance moment coefficient for the rotor wetted by the liquid on two sides is calculated by the formula

$$C_M = \frac{4M}{\rho\omega^2 b^5} = 4\pi \int\limits_{a/b}^{1} \left(\frac{r}{b}\right)^2 \frac{\tau_{x\theta}}{\rho\omega^2 b^2}\, d\left(\frac{r}{b}\right).$$

The dependence of the moment coefficient on the dimensionless width of the cavity has a minimum (Fig. 5). The critical width of the gap is temperature-dependent ($G_* = 0.0132$ for $T_2 = 300$ K and $G_* = 0.0145$ for $T_2 = 400$ K).

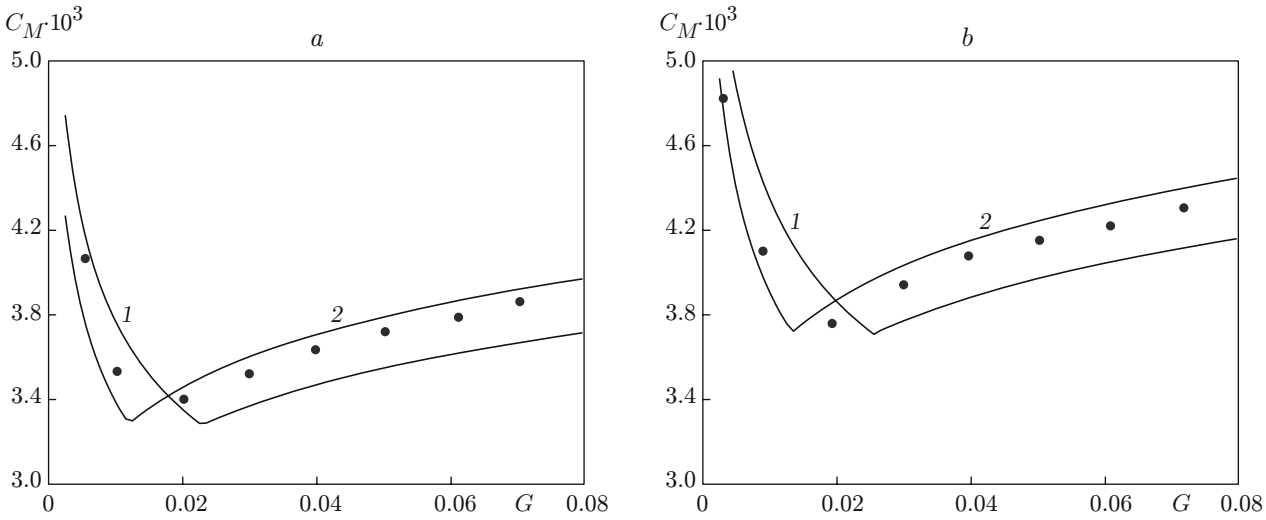

Fig. 5. Moment coefficient versus the dimensionless gap between the stator and rotor for $\mathrm{Re} = 4.4 \cdot 10^6$, and $T_2 = 300$ K (a) and $\mathrm{Re} = 2.5 \cdot 10^6$ and $T_2 = 400$ K (b): curves 1 and 2 refer to the correlations derived in [1] and [2], respectively; the points are the results of numerical simulations.

TABLE 1

Moment and Moment Coefficient
Calculated on the Basis of Different Turbulence Models for $T_2 = 450$ K

Model	M, N · m	$C_M \cdot 10^3$	δ, %
k–ε	2.3026	3.5115	8.79
k–ε/k–l	2.4138	3.7125	4.39
k–ω	2.2350	3.4376	11.47
SA1	2.1972	3.3795	12.96
SA2	2.2325	3.6637	5.64
RSM	2.3729	3.6496	6.01
[1]	2.3624	3.6335	6.4
[2]	2.5245	3.8828	—

The moment for the free disk is greater than the moment for the disk in the shroud. The disk rotating in the shroud has a lower moment because the angular velocity of the liquid between two boundary layers on each side of the disk is half the angular velocity of the disk. For this reason, the gradients of circumferential velocity are twice lower than those for the free disk, and the friction forces for the disk in the shroud are smaller than those for the free disk.

The results calculated with the use of different turbulence models are summarized in Table 1. The third column of Table 1 shows the calculation error C_M for different turbulence models with respect to the dependence given in [2]. The best agreement with the data of the physical experiment is ensured by using the two-layer turbulence model and the model of the Reynolds stress transport. The latter model, however, requires approximately 40% of computational time more than two-parameter turbulence models.

Conclusions. The turbulent flow and heat transfer in a closed axisymmetric cavity with a rotating disk is modeled. The flow structure and friction parameters are examined as functions of the dimensionless gap between the motionless casing and rotating disk and of the Reynolds number. A comparison of the calculated results with the data of a physical experiment and available correlations shows that the best agreement is ensured by the two-layer k–ε/k–l turbulence model. The use of corrections for the term related to turbulence generation and streamline curvature improves the properties of the standard k–ε model.

REFERENCES

1. J. W. Daily and R. Nece, "Chamber dimension effects on induced flow and frictional resistance of enclosed rotating discs," *Trans. ASME, J. Basic Eng.*, **82**, 217–232 (1960).
2. F. Kreith, "Convection heat transfer in rotating systems," *Adv. Heat Transfer*, **5**, 129–251 (1968).
3. J. M. Owen and R. H. Rogers, *Flow and Heat Transfer in Rotating-Disc Systems*. Rotating Cavities, Research Studies Press, Taunton (1995).
4. G. Schlichting, *Boundary Layer Theory*, McGraw-Hill, New York (1968).
5. R. Jacques, P. Le Quere, and O. Daube, "Axisymmetric numerical simulations of turbulent flow in rotor stator enclosures," *Int. J. Heat Fluid Flow*, **23**, 381–397 (2002).
6. G. P. Beretta and E. Malfa, "Flow and heat transfer in cavities between rotor and stator disks," *Int. J. Heat Mass Transfer*, **46**, 2715–2726 (2003).
7. H. Iacovides and P. Toumpanakis, "Turbulence modeling of flow in axisymmetric rotor-stator systems," in: *Proc. of the 5th Int. Symp. on Refined Flow Modelling and Turbulence Measurements* (Paris, France, September 7–10, 1993), Presses de l'Ecole Nationale des Ponts et Chaussées, Paris (1993), pp. 383–390.
8. A. P. Morse, "Numerical prediction of turbulent flow in rotating cavities," *Trans. ASME, J. Turbomach.*, **110**, 202–212 (1988).
9. M. Djaoui, A. Dyment, and R. Debuchy, "Heat transfer in a rotor–stator system with a radial inflow," *Europ. J. Mech., B: Fluids*, **20**, 371–398 (2001).
10. L. Elena and R. Schiestel, "Turbulence modeling of rotating confined flows," *Int. J. Heat Fluid Flow*, **17**, 283–289 (1996).
11. B. E. Launder and D. B. Spalding, "The numerical computation of turbulent flows," *Comput. Meth. Appl. Mech. Eng.*, **3**, 269–289 (1974).
12. M. Kato and B. E. Launder, "The modelling of turbulent flow around stationary and vibrating square cylinders," in: *Proc. of the 9th Symp. on Turbulent Shear Flows* (Kyoto, Japan, August 16–18, 1993), Vol. 9, S. n. (1993), pp. 10.4.1–10.4.6.
13. M. A. Leschziner and W. Rodi, "Calculation of annular and twin parallel jets using various discretization schemes and turbulent-model variations," *Trans. ASME, J. Fluids Eng.*, **103**, 353–360 (1981).
14. W. Rodi, "Experience with two-layer models combining the k–ε model with one-equation model near wall," AIAA Paper No. 91-0216 (1991).
15. D. C. Wilcox, "A two-equation turbulence model for wall-bounded and free-shear flows," AIAA Paper No. 93-2905 (1993).
16. P. R. Spalart and S. R. Allmaras, "A one equation turbulence model for aerodynamic flows," AIAA Paper No. 92-0439 (1992).
17. J. Dacles-Mariani, G. G. Zilliac, J. S. Chow, and P. Bradshaw, "Numerical/experimental study of a wingtip vortex in the near field," *AIAA J.*, **33**, No. 9, 1561–1568 (1995).
18. S. Deck, P. Duveau, P. d'Espiney, and P. Guillen, "Development and application of Spalart–Allmaras one-equation turbulence model to three-dimensional supersonic complex configurations," *Aerospace Sci. Technol.*, **6**, 171–183 (2002).
19. W. P. Jones and P. Musonge, "Closure of the Reynolds stress and scalar flux equations," *Phys. Fluids*, **31**, No. 12, 3589–3604 (1988).